

# PHOTONICS Research

## Low temperature sensitivity on-chip Fourier-transform spectrometer based on dual-layer Si<sub>3</sub>N<sub>4</sub> spiral waveguides

LIANGJUN LU,<sup>1,2,†,\*</sup>  HONGYI ZHANG,<sup>1,†</sup> XIN LI,<sup>1</sup> JIANPING CHEN,<sup>1,2</sup> AND LINJIE ZHOU<sup>1,2</sup>

<sup>1</sup>State Key Laboratory of Advanced Optical Communication Systems and Networks, Shanghai Key Laboratory of Navigation and Location Services, Department of Electronic Engineering, Shanghai Jiao Tong University, Shanghai 200240, China

<sup>2</sup>SJTU-Pinghu Institute of Intelligent Optoelectronics, Pinghu 314200, China

\*Corresponding author: luliangjun@sjtu.edu.cn

Received 13 December 2022; revised 29 January 2023; accepted 11 February 2023; posted 13 February 2023 (Doc. ID 483540); published 27 March 2023

On-chip Fourier-transform spectrometers (FTSs) based on Mach–Zehnder interferometer (MZI) arrays suffer from severe central wavelength and fringe contrast variation due to fabrication errors. Even though a calibration matrix can be employed to correctly retrieve the input spectra, environmental temperature variation greatly degrades the retrieving performance. In this paper, we devise a dual-layer Si<sub>3</sub>N<sub>4</sub> waveguide interferometer to reduce the temperature sensitivity. The beating of the even and odd supermodes in the dual-layer waveguide generates periodic intensity fluctuations in the spectrum. Since these two modes have similar modal profiles, their thermal sensitivity and propagation loss are relatively balanced, leading to a low temperature sensitivity and a high interference extinction ratio. We designed and fabricated a passive FTS based on a 32-channel dual-layer Si<sub>3</sub>N<sub>4</sub> waveguide array. Experimental results show that the temperature sensitivity is reduced to 10 pm/°C, which is almost half that of single-layer Si<sub>3</sub>N<sub>4</sub> MZI-based FTSs. With this chip, we accurately reconstructed various types of optical spectra, including single and two sparse laser lines, and broadband optical spectra. Our method can fit a wide wavelength range, which is a promising technology to improve the practical applications of on-chip FTSs. © 2023 Chinese Laser Press

<https://doi.org/10.1364/PRJ.483540>

### 1. INTRODUCTION

Miniaturized optical spectrometers have wide applications, such as spectroscopic sensing, optical network performance monitoring, hyperspectral imaging, and radio frequency spectrum analysis, and offer dramatic size, weight, and power reductions [1–3]. Among various types of miniaturized optical spectrometers, on-chip Fourier-transform spectrometers (FTSs), which use interferometers to modulate the input light to generate interferograms, and retrieve the spectrum via the Fourier transform, are regarded as a promising technology for high-resolution, compact optical spectrometers. With the intrinsic advantages of silicon photonics, silicon-based FTSs can further reduce the device size as well as the cost, due to their high index contrast and CMOS compatibility. Recently, various on-chip FTSs have been demonstrated based on a Mach–Zehnder interferometer (MZI) array with various optical path differences (OPDs) [4–8], which is one of the most common optical components used in photonic integration. The MZI array modulates the input light into spatially distributed interferograms, which are analogous to conventional

Michelson interferometer-type FTSs. The resolution can be enhanced either by increasing the OPDs or by using advanced spectral retrieving algorithms, like compressive sensing and machine learning [9–12]. Besides the communications band, on-chip FTSs have also been demonstrated for the mid-IR band [13–16]. Some of the works are also focused on approaches to improve the tunability or the scalability of MZIs to get a higher spectral resolution. For example, with cascaded optical switches to reconfigure the MZI arm length, the OPD can be digitally tuned to realize high-resolution scalable FTSs [17–19]. Upon thermo-optic or electro-optic modulation of one of the MZI arms, the OPD can also be continuously tuned and, in this case, it only needs one MZI to realize the FTS [20–22].

Conventionally, due to fabrication errors, the central wavelength and the fringe contrast of FTSs deviate from the design. Therefore, a calibration matrix is required to retrieve the input spectrum. The accuracy of the calibration matrix determines the correctness of the retrieved spectrum. However, silicon has a relatively large thermo-optic coefficient (TOC), which makes silicon photonic devices sensitive to environmental temperatures. Typically, the thermal sensitivity is about 100 pm/K.

The environmental temperature variation in the calibration and the spectrum measurement results in deviation of the retrieved spectrum. It greatly limits the practical usage of such on-chip FTSs, especially when the resolution is very high. One way to reduce the temperature sensitivity is to use asymmetric MZIs with different arm widths and lengths to cancel the temperature-dependent phase difference between the two MZI arms [23–25]. However, the temperature-insensitive operation bandwidth is very narrow. A subwavelength grating (SWG) structure can engineer the dispersion of the waveguide, and thus can enhance the operation bandwidth [26]. However, it typically requires high-resolution electron beam lithography (EBL) to pattern the subwavelength gratings. Another way is to use negative TOC material as the waveguide upper cladding to cancel the positive TOC of the silicon waveguide core [27–29]. All the above methods need precise waveguide dimension control to eliminate temperature-induced degradation.

The second issue is the visibility of the interferogram. Typically, the extinction ratio (ER) of an asymmetric MZI is dependent on the power-splitting uniformity of the 3 dB couplers and the loss difference between the two arms. It is possible to realize high-performance, 3 dB couplers with both low power imbalance and a broad bandwidth based on an adiabatic design [30,31]. However, as the OPD of the MZI increases, the transmission loss difference between the two arms inevitably increases due to fabrication imperfection. As a result, the ER of the MZI decreases with the OPD. The reduced fringe visibility degrades the dynamic range of the spectral measurement.

Here, we propose and demonstrate what we believe, to the best of our knowledge, is a novel FTS based on a dual-layer  $\text{Si}_3\text{N}_4$  spiral waveguide array. Two supermodes with different group indices are excited and interfere in the dual-layer  $\text{Si}_3\text{N}_4$  waveguides, generating periodic spectral fringes. The TOC and propagation loss of the two supermodes are similar. Therefore, the temperature sensitivity and the ER of the waveguide interferometric structure are improved. With our chip, we successfully recover various types of input spectra, including single/dual separate laser lines and a broad optical signal.

## 2. DEVICE STRUCTURE AND WORKING PRINCIPLE

### A. Dual-Layer Waveguide Interferometers

Figure 1(a) shows the cross-sectional view of the dual-layer  $\text{Si}_3\text{N}_4$  waveguide. Two layers of silicon nitride waveguides with the same dimensions ( $1000 \text{ nm} \times 400 \text{ nm}$ ) are stacked vertically with a separation gap of  $200 \text{ nm}$ . Figure 1(b) presents the simulated electric field intensity profiles (TE polarization) of the even and odd supermodes of the dual-layer waveguide. The dual-layer  $\text{Si}_3\text{N}_4$  waveguide can be regarded as a vertically coupled directional coupler (DC). Planar DCs have been widely used as power splitters. As we know, the working principle of a DC can be understood as the beating of even and odd supermodes in the composite waveguide, leading to optical intensity oscillation along the propagation direction. The beating length is inversely proportional to the difference of the propagation constants (or the effective indices) of the two supermodes. Conventionally, power splitters must process a large operational bandwidth. However, in our device, we use its interference effect to discriminate the frequency component of an input signal; therefore, its length is much longer than the crossing-coupling length so that a dense periodic interference spectrum results.

This periodic spectral response of the DCs is beneficial for the FTS application. The two supermodes have different group indices of  $n_{ge}$  and  $n_{go}$ , and the OPD of the dual-layer waveguide structure is given by  $|n_{ge} - n_{go}|L$ , where  $L$  is the waveguide length. Hence, the free spectral range (FSR) is  $\lambda_0^2/|n_{ge} - n_{go}|L$ , where  $\lambda_0$  is the central wavelength of the input light in the vacuum. The group index difference between the two supermodes can be optimized by the waveguide geometry of the dual-layer  $\text{Si}_3\text{N}_4$  waveguide. The FSR of the interference is related to the FTS resolution and the operation bandwidth.

To excite and split these two supermodes, we added two interlayer Y junctions at the input and output ends of the dual-layer  $\text{Si}_3\text{N}_4$  waveguide. Figure 1(c) presents the schematic structure of the holistic dual-layer  $\text{Si}_3\text{N}_4$  waveguide

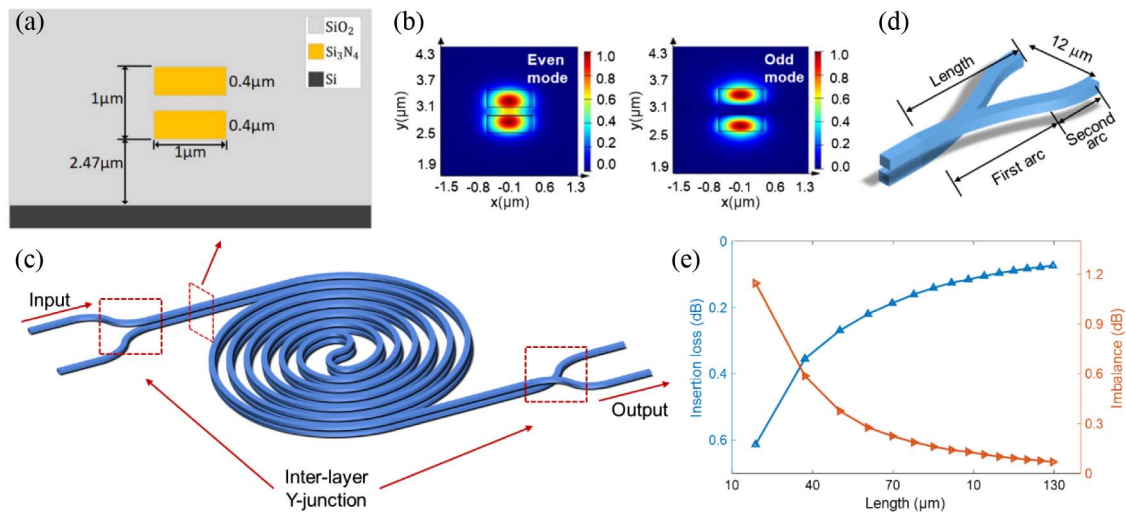


**Fig. 1.** (a) Cross-section of the dual-layer  $\text{Si}_3\text{N}_4$  waveguide. (b) Electric field intensity distribution of the even and odd supermodes of the dual-layer  $\text{Si}_3\text{N}_4$  waveguide. (c) Schematic of the spiral-shaped dual-layer  $\text{Si}_3\text{N}_4$  waveguide interferometer. (d) Schematic structure of the interlayer Y junction. (e) Simulated insertion loss and power imbalance of the interlayer Y junction under various lengths.

interferometer. The dual-layer  $\text{Si}_3\text{N}_4$  waveguide is arranged in a spiral shape to reduce the chip footprint. This is the advantage of dual-layer waveguides over planar DCs. Light from the upper (bottom) branch of the input interlayer Y junction can be evenly split into the even and odd supermodes at the junction. The interference of the two supermodes in the dual-layer waveguide results in the optical intensity oscillation along the propagation direction. At the output interlayer Y junction, the optical power in the two layers is divided. Therefore, the detected power from either single-layer  $\text{Si}_3\text{N}_4$  waveguide is oscillatory with respect to the wavelength. The interlayer Y junction works as a 3 dB coupler and the entire dual-layer  $\text{Si}_3\text{N}_4$  waveguide interferometer resembles an asymmetric MZI commonly used in FTS chips.

Figure 1(d) shows the structure of the interlayer Y junction, which is formed by two  $\text{Si}_3\text{N}_4$  layers. The Y junction is simply designed with two arcs in both the upper and lower branches. Typically, the junction part should be carefully designed to realize adiabatic mode evolution. However, in our design, we only set the bending radius of the interlayer Y junctions as  $60\ \mu\text{m}$ , which results in a large power imbalance, and thus a reduced ER. Figure 1(e) shows the 3D finite-difference time-domain (FDTD) simulation results of the interlayer Y junction. In the simulation, light is launched into the upper branch of the Y junction, so it splits into even and odd supermodes at the output port. We monitored the output transmission of these two supermodes. Since the first arc decides the splitting speed of the two branches, we just varied the bending radius of the first arc while fixing the bending radius of the second arc and the spacing of the two ports as  $60\ \mu\text{m}$  and  $12\ \mu\text{m}$ , respectively. By increasing the bending radius of the first arc, the loss in the mode evolution is reduced, but the length of the Y junction also increases accordingly. As shown in Fig. 1(e), the insertion loss is 0.61 dB for the Y junction length of  $18.9\ \mu\text{m}$ , which corresponds to the bending radius of  $60\ \mu\text{m}$  used in our chip. It can be reduced to 0.07 dB when the length of the Y junction increases to  $130\ \mu\text{m}$ . The power imbalance is defined as the power ratio of these two supermodes in decibels. It can also be improved from 1.15 dB to 0.07 dB by increasing the length of the Y junction. To further reduce the length of the Y junction, we can optimize the shape of the arc by using the particle swarm optimization (PSO) method [32].

## B. Temperature Sensitivity and ER Analysis

The temperature sensitivity of a conventional single-layer MZI can be expressed as the wavelength shift upon temperature variation, which is given by [33,34]

$$\frac{\partial\lambda}{\partial T} = \frac{\lambda_0}{n_g} \frac{\partial n_{\text{eff}}}{\partial T}, \quad (1)$$

where  $\partial n_{\text{eff}}/\partial T$  and  $n_g$  are the TOC and the group index of the waveguide. The TOC of a  $\text{Si}_3\text{N}_4$  waveguide can be expressed as [29]

$$\frac{\partial n_{\text{eff}}}{\partial T} = \Gamma_{\text{Si}_3\text{N}_4} \frac{\partial n_{\text{Si}_3\text{N}_4}}{\partial T} + \Gamma_{\text{SiO}_2} \frac{\partial n_{\text{SiO}_2}}{\partial T}, \quad (2)$$

where  $\Gamma$  and  $\partial n/\partial T$  are the confinement factor and the material TOC. The thermal sensitivity of the single-layer MZI is highly dependent on the waveguide's TOC. By using

$\text{Si}_3\text{N}_4$  instead of Si as the waveguide core, the thermal sensitivity can be reduced because of the lower  $\text{Si}_3\text{N}_4$  TOC as well as its lower mode confinement. For our dual-layer  $\text{Si}_3\text{N}_4$  waveguide interferometer, the temperature sensitivity can be revised as

$$\frac{\partial\lambda}{\partial T} = \frac{\lambda_0}{\Delta n_g} \frac{\partial \Delta n_{\text{eff}}}{\partial T} = \frac{\lambda_0}{n_{\text{go}} - n_{\text{gc}}} \left( \frac{\partial n_{\text{effo}}}{\partial T} - \frac{\partial n_{\text{effe}}}{\partial T} \right), \quad (3)$$

where  $\partial \Delta n_{\text{eff}}/\partial T$  is the difference of the TOC of the odd mode ( $\partial n_{\text{effo}}/\partial T$ ) and the even mode ( $\partial n_{\text{effe}}/\partial T$ ). The TOC difference relates to the temperature-dependent phase difference of the dual-layer  $\text{Si}_3\text{N}_4$  waveguide structure. As can be seen in Fig. 1(c), the confinement factors in the  $\text{Si}_3\text{N}_4$  core of the two supermodes are very close, which means the TOC difference is very small. By proper dimension design of the dual-layer waveguide, the confinement factors of the two supermodes can be identical; thus, the temperature sensitivity of the structure can be completely canceled.

Figure 2(a) shows the simulated group index difference and temperature sensitivity of the dual-layer waveguide under different waveguide widths and separation gaps at a wavelength of  $1.56\ \mu\text{m}$ . In the simulation, the TOC values of  $\text{Si}_3\text{N}_4$  and  $\text{SiO}_2$  are set as  $2.6 \times 10^{-5}$  and  $1 \times 10^{-5}\ \text{°C}^{-1}$ , and the refractive indices of  $\text{Si}_3\text{N}_4$  and  $\text{SiO}_2$  are 1.99 and 1.444, respectively. The group index is calculated based on the finite difference eigenmode (FDE) method by the Ansys Lumerical MODE solution, and  $\Delta n_g$  is calculated as  $n_{\text{gc}} - n_{\text{go}}$ . The waveguide TOC is calculated by Eq. (2), and the confinement factor is calculated based on Ref. [35]. In comparison, Fig. 2(b) shows the simulated group index and temperature sensitivity of the single-layer MZI. For the regular MZI structure based on single-layer  $\text{Si}_3\text{N}_4$  waveguides, the temperature sensitivity slightly increases with the waveguide width because more light is confined in the  $\text{Si}_3\text{N}_4$ . The temperature sensitivity is  $\sim 17.9\ \text{pm}/\text{°C}$  for a waveguide width of  $1\ \mu\text{m}$ . In contrast, with an increase in the waveguide width, the temperature sensitivity of the dual-layer waveguide interferometer changes from negative to positive and reaches the temperature-insensitive point with a proper waveguide width. In addition, as the separation gap increases from  $0.2$  to  $0.3\ \mu\text{m}$ , the temperature-insensitive waveguide width decreases accordingly. In this work, we chose the separation gap as  $0.2\ \mu\text{m}$  to be compatible with other designs in this multilayer  $\text{Si}_3\text{N}_4$ -on-SOI (silicon on insulator) platform [36,37]. The absolute value of  $\Delta n_g$  of the dual-layer waveguide increases with the waveguide width and is almost stable when the waveguide width is larger than  $1.4\ \mu\text{m}$ . Since the group index difference at the temperature-insensitivity point is relatively small, as illustrated by the orange dashed line in Fig. 2(a), we choose a width of  $1\ \mu\text{m}$  to balance the chip size and the temperature sensitivity of our FTS chip. The temperature sensitivity is  $\sim 11\ \text{pm}/\text{°C}$ . The temperature response can be flexibly tailored by the waveguide geometry of the dual-layer waveguide. Since  $\text{Si}_3\text{N}_4$  is transparent over a wide wavelength range, it is also easy to extend the operation wavelength using the dual-layer waveguide structure.

Besides the thermal stability, the contrast of the interference fringes is also very important for the accurate reconstruction of the input spectrum. However, as the OPD of the MZI

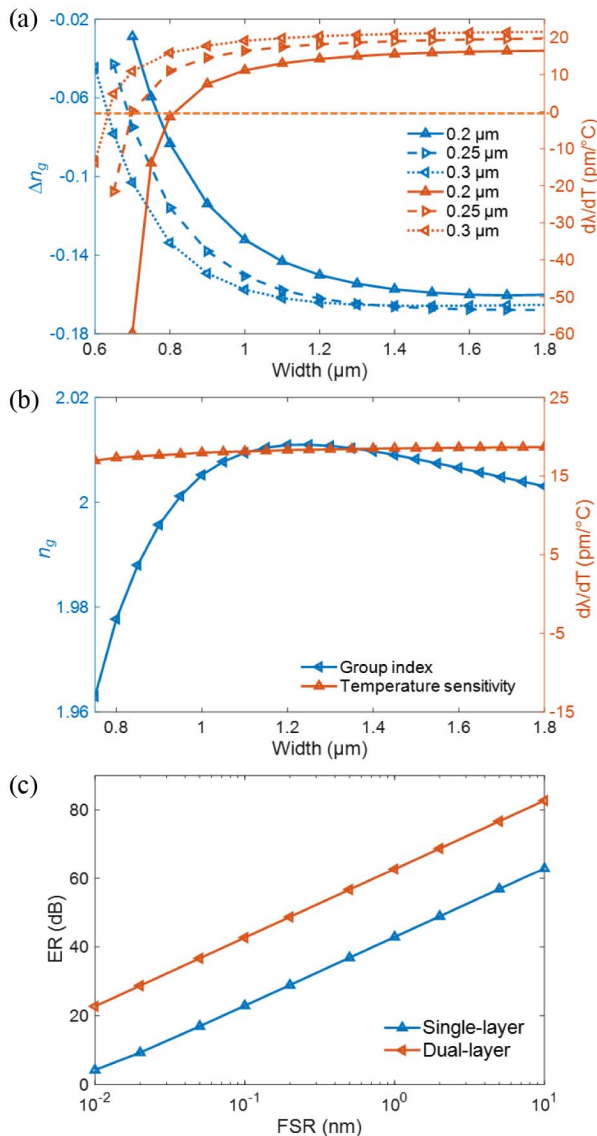


**Fig. 2.** (a) Group index difference and temperature sensitivity of the dual-layer  $\text{Si}_3\text{N}_4$  waveguide when the separation gap changes from 0.2 to 0.3  $\mu\text{m}$ . (b) Group index and temperature sensitivity of the single-layer MZI. (c) Extinction ratio of the two interferometer structures as a function of the FSR.

increases, the length difference between the two arms increases, which increases the loss difference and degrades the ER. As for our dual-layer  $\text{Si}_3\text{N}_4$  waveguide interferometer, the propagation length of the two interference modes is equal. Since the mode profiles of these two modes are similar, the loss difference between these two modes is greatly suppressed. Higher fringe contrast can be achieved with our waveguide structure. Figure 2(c) shows the simulated ERs of our dual-layer waveguide interferometer and the single-layer MZI structure under different FSRs. In the simulation, the extinction coefficient of  $\text{Si}_3\text{N}_4$  is set to be  $4 \times 10^{-6}$ , corresponding to a 1.026 dB/cm loss for a single-layer waveguide, and 1.059 dB/cm and 1.066 dB/cm for the even and odd modes of the dual-layer waveguide. The 3 dB coupler is considered as perfectly 50:50. We can see that even though the required length of the

dual-layer waveguide is longer than that of an MZI for the same FSR, the ER of the dual-layer waveguide is almost 20 dB larger than that of the regular MZI. Therefore, it reveals that dual-layer waveguide structures also have better performance in fringe contrast.

### C. FTS Chip Design and Fabrication

To demonstrate its performance, we designed a passive FTS chip consisting of a 32-channel dual-layer  $\text{Si}_3\text{N}_4$  waveguide interferometer array with a linearly increased waveguide length. The input light is evenly split into 32 channels by five stages of  $1 \times 2$  power splitters. The  $1 \times 2$  power splitters are based on multimode interference (MMI) structures and implemented in the upper  $\text{Si}_3\text{N}_4$  layer. The outputs of the  $1 \times 2$  MMI power splitters are connected to the upper input ports of the interlayer Y junctions to evenly excite the even and odd supermodes in the dual-layer  $\text{Si}_3\text{N}_4$  waveguide. The minimum length of the dual-layer waveguides is 1200  $\mu\text{m}$ , and the length is increased with a step of 1200  $\mu\text{m}$ . Therefore, the optical bandwidth is 7.67 nm and the spectral resolution is 0.48 nm. To reduce the footprint, these waveguides are designed in a spiral shape with a minimum bending radius of 60  $\mu\text{m}$ , as shown in Fig. 1(c). The bending radius can be further reduced using an Euler-bend design [38]. At the output port of each spiral waveguide, another interlayer Y junction converts the modes of the dual-layer waveguide into two separated modes in the upper and the bottom  $\text{Si}_3\text{N}_4$  layers. The upper-layer waveguides are used for optical power measurement. The other ports of the Y junctions are routed to silicon grating couplers by interlayer couplers, which are used as test ports.

The fabrication of the chip starts from an 8-inch SOI wafer with a 220 nm thick top silicon layer and 3  $\mu\text{m}$  thick bottom oxide layer. The  $\text{Si}_3\text{N}_4$  layers were deposited by low-pressure chemical vapor deposition (LPCVD) and flattened by chemical-mechanical polishing (CMP). The silicon and the  $\text{Si}_3\text{N}_4$  waveguides were patterned by 248 nm deep UV (DUV) lithography followed by dry etching. The whole chip was fabricated by the Shanghai Industrial  $\mu$ Technology Research Institute (SITRI). Figure 3(a) shows the microscope image of the fabricated chip. The footprint of the chip is 5.8 mm  $\times$  4.6 mm. Figure 3(b) shows the SEM image of the dual-layer  $\text{Si}_3\text{N}_4$  waveguide. The etched waveguide angle is about 82°. Input and output fiber couplers are based on  $\text{Si}_3\text{N}_4$  inverse tapers with a tip width of 200 nm, all arranged on the left edge of the chip. Two U-shaped bending waveguides are used to assist the coupling with a 37-channel fiber array. The coupling loss is  $\sim 5$  dB/facet. Figure 3(c) shows the FTS chip after the optical package. The chip was packaged by SJTU-Pinghu Institute of Intelligent Optoelectronics.

## 3. EXPERIMENTAL RESULTS

### A. Thermal Sensitivity Measurement

We characterized the thermal sensitivity of our dual-layer  $\text{Si}_3\text{N}_4$  waveguide. For comparison, we also measured the thermal sensitivity of two microring resonators (MRRs) made of single-layer  $\text{Si}_3\text{N}_4$  waveguides in the upper and bottom layers. The waveguide width is also 1  $\mu\text{m}$ . Figures 4(a)–4(c) show the measured transmission spectra of these three test devices when

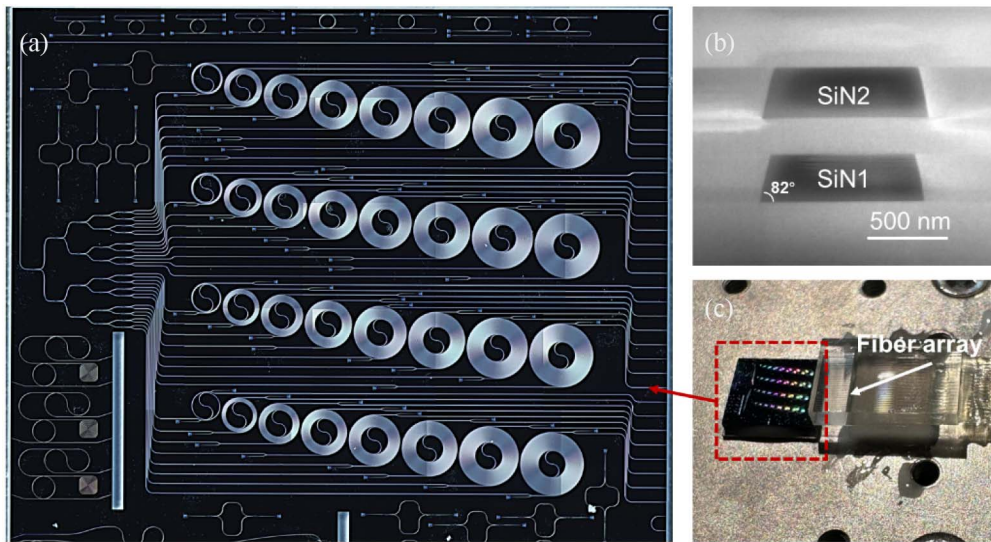


**Fig. 3.** (a) Microscope image of the fabricated chip. (b) SEM image of the dual-layer waveguide cross-section. (c) Picture of the packaged chip.

the temperature increases from 20°C to 60°C. The extracted central wavelength shifts are shown in Figs. 4(d)–4(f). We can see that the thermal sensitivities of our dual-layer Si<sub>3</sub>N<sub>4</sub> waveguide and the single-layer MRRs are ~10 pm/°C and 17.8 pm/°C, respectively, which is consistent with the simulation. The temperature-dependent wavelength shift is one order lower than the Si waveguide, and almost half that of the single-layer Si<sub>3</sub>N<sub>4</sub> waveguide, which verifies that our FTS chip has low temperature sensitivity.

**B. Calibration and Reconstruction Method**

To correct the fabrication imperfection-induced deviation of the periodic fringes in the dual-layer Si<sub>3</sub>N<sub>4</sub> waveguide arrays,

a calibration matrix was needed for spectral reconstruction. We measured the transmission spectra of the 32 waveguide interferometers using a tunable laser scanned from 1554 to 1566 nm wavelength with a step of 10 pm. The input power was set to 0 dBm. A group of 32-channel power meters were used to record the optical power from the 32 output ports of the waveguide interferometer array. Note that since our chip has high temperature stability, we did not use a thermoelectric cooler (TEC) in both the calibration and the spectral interrogation. Figures 5(a) and 5(b) show the measured spectra of the dual-layer spiral waveguide interferometers with the shortest and the longest waveguide lengths of 1.2 mm and 38.4 mm, respectively. The FSR of the longest waveguide interferometer

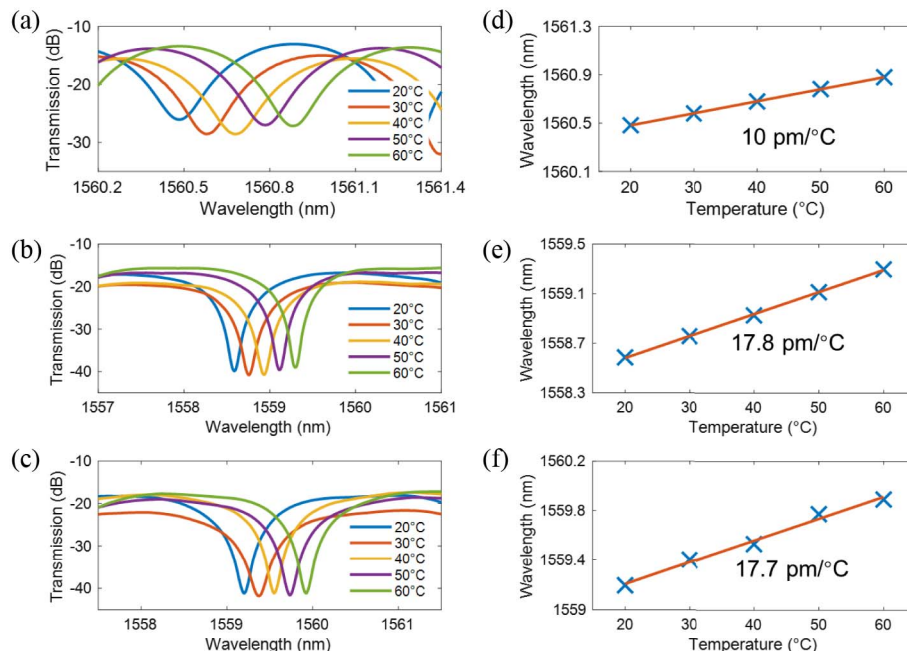


**Fig. 4.** (a)–(c) Measured transmission spectra and (d)–(f) extracted central wavelength shift under various temperatures. (a) and (d) Dual-layer Si<sub>3</sub>N<sub>4</sub> spiral waveguide; (b) and (e) MRR in the upper Si<sub>3</sub>N<sub>4</sub> layer; and (c) and (f) MRR in the bottom Si<sub>3</sub>N<sub>4</sub> layer.

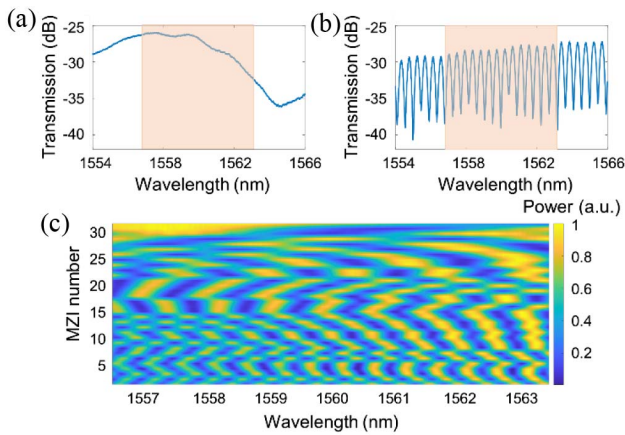


**Fig. 5.** (a) and (b) Measured transmission spectra of (a) the shortest and (b) the longest dual-layer spiral waveguide interferometers of the FTS chip. The pink-shaded areas illustrate the wavelength range for spectral reconstruction. (c) Normalized calibration matrix obtained by a tunable laser.

is  $\sim 0.46$  nm. The ER difference is negligible for the two waveguide interferometers. However, as mentioned above, the unoptimized interlayer Y junctions result in a relatively large power imbalance of the two supermodes, lowering the ER to  $\sim 12$  dB over the measured wavelength range.

We used the spectra in the wavelength range from 1556.5 to 1563.5 nm to construct the calibration matrix, which is slightly smaller than the operation bandwidth of our chip. The size of the calibration matrix  $\hat{A}$  is  $32 \times 701$ , with each row representing the spectral response of each waveguide interferometer in the FTS chip. To improve the spectral reconstruction, the measured transmission spectra were normalized with the maximum power for each interferometer, which is expressed as

$$A_{i,j} = \hat{A}_{i,j} / \max(\hat{A}_{i,j} = 1:701), \quad (4)$$

where  $A$  is the normalized calibration matrix. Figure 5(c) displays the normalized calibration matrix, with each row representing the spectrum of a dual-layer waveguide interferometer.

In the spectral reconstruction, the tunable laser was replaced by an unknown input optical signal. The measured output power  $\hat{y}$  by the power meter was also normalized as

$$y_i = \hat{y}_i / \max(\hat{A}_{i,j} = 1:701), \quad (5)$$

where  $y$  is a column vector with 32 elements representing the normalized output power. The input unknown spectrum  $x$  can be expressed as a column vector consisting of 701 elements. The reconstruction of the unknown spectrum is to solve the vector  $x$  from

$$y = Ax. \quad (6)$$

We applied the elastic- $D_1$  regularization regression algorithm to retrieve the spectra  $x$ , which has been proven as a powerful algorithm for both sparse and broadband spectra [17]. The objective function of the elastic- $D_1$  is expressed as

$$\min_{x, x > 0} \{ \|y - Ax\|_2^2 + \alpha_1 \|x\|_1 + \alpha_2 \|x\|_2^2 + \alpha_3 \|D_1 x\|_2^2 \}, \quad (7)$$

where  $\alpha_i$  ( $i = 1, 2, 3$ ) is the hyperparameter for each penalty term. We solved the equation above with standard convex optimization tools [17].

### C. Spectral Reconstruction Results

We first evaluated the reconstruction ability for sparse spectra with a single laser line and two separate laser lines. The sparse laser lines were generated by one or two tunable laser sources, and the input power was set to 0 dBm. Figure 6(a) shows the reconstructed spectra of the input single-line laser. The input light changes from 1559 to 1559.96 nm with a step of 0.08 nm. The wavelengths of all the spectral lines are accurately recovered by our FTS chip, and the amplitudes are close to 1, indicating the good reconstruction performance of our chip. Figures 6(b)–6(f) show the results of two laser lines when the wavelength spacing increases from 0.2 to 1 nm with a step of 0.2 nm. When the spacing is above 0.2 nm, the two lines are clearly distinguished from each other, and the retrieved wavelengths match with the results from a benchtop optical spectrum analyzer (AQ63700, Yokogawa Electric), as illustrated by the orange dashed lines. However, splitting peaks are observed in Fig. 6(b) when the spacing is 0.2 nm, due to

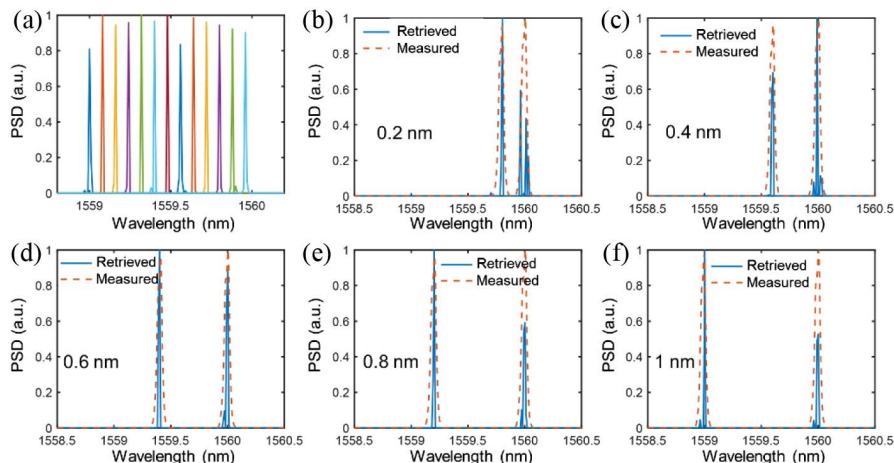


**Fig. 6.** (a) Reconstructed spectra of the single narrowband laser source. (b)–(f) Measured and reconstructed spectra of the two narrowband laser sources with a wavelength spacing of (b) 0.2 nm, (c) 0.4 nm, (d) 0.6 nm, (e) 0.8 nm, and (f) 1 nm. PSD, power spectral density.

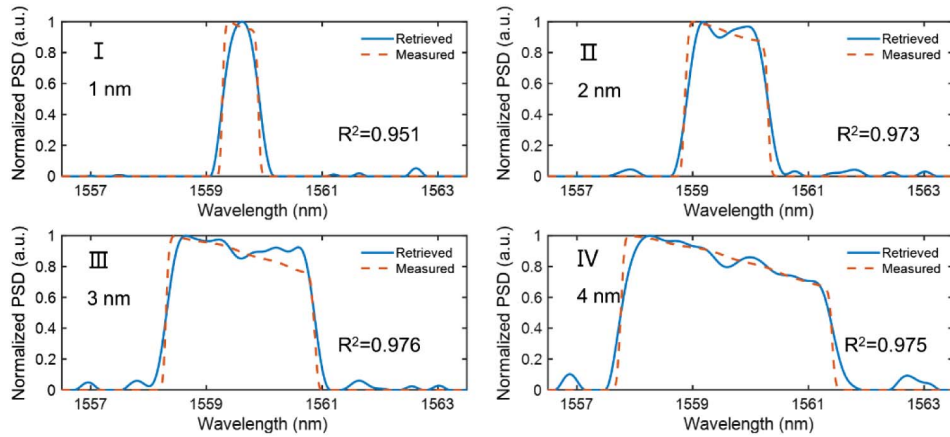


**Fig. 7.** Measured and reconstructed spectra of a broadband optical signal with the bandwidth increasing from 1 to 4 nm. PSD, power spectral density.

the limited resolution of our FTS chip. There also are a few peaks in the retrieved spectrum around the 1560 nm wavelength, which influences the retrieved amplitude of the sparse signal. The limited ER of our FTS chip reduces the discrimination of the wavelength position and therefore generates several wavelength components near the central wavelengths. In the future, we can increase the ER of the FTS by increasing the bending radius of the interlayer Y junctions and further improving the spectral resolution by increasing the length of the dual-layer waveguides and the number of waveguides in the array.

We also characterized the reconstruction performance for broadband optical spectra. The input spectrum was generated using an amplified spontaneous emission (ASE) light source and a tunable optical bandpass filter. The bandwidth of the filter was tuned, and the bandwidth of the input optical signal varied from 1 to 4 nm. To better evaluate the reconstruction performance, we normalized both the retrieved spectra and the measured spectra to the maximum. Figure 7 shows the reconstructed results with our on-chip spectrometer. As observed, the reconstructed envelope shape fits the measured shape very well. The slant optical passbands are due to the ASE light source. The  $R^2$  value calculated from the reconstructed and the measured spectra is close to 1, indicating good reconstruction performance.

Finally, we implemented the spectral reconstruction for a single-line laser source at the 1560 nm wavelength and a broadband optical signal with a bandwidth of 1 nm under various temperatures. The temperature was adjusted by a TEC, and the calibration matrix was obtained at the initial temperature. The reconstruction algorithm was also based on the elastic- $D_1$  regularization method. Figure 8(a) shows the reconstruction results for a single-line laser source. We can see that with the increased temperature deviation, a shorter wavelength line rises from the reconstructed spectrum. When the temperature deviation reached 1.4°C, the amplitude of the shorter wavelength line was almost close to the original laser line. Since the calibration matrix is fixed, and the temperature variation causes a red shift of the output spectrum of the waveguide interferometers, the wavelength position of the recovered spectrum

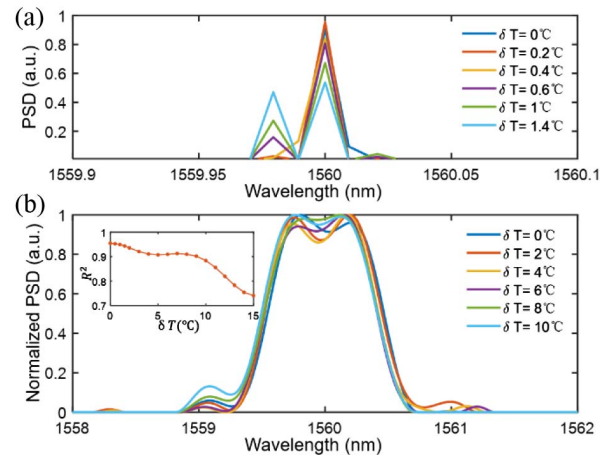


**Fig. 8.** Reconstructed spectra of (a) the single-line laser source and (b) the broadband optical signal under various temperatures.

shifts to the blue side. Figure 8(b) shows the reconstructed spectra for the broadband optical signal. The central wavelength and the envelope of the reconstructed signal change slightly, even with a 10°C temperature variation. We used the  $R^2$  value under various temperatures to determine the fidelity of the retrieved spectrum. When the temperature variation is less than 5°C, the  $R^2$  value is larger than 0.9.

#### 4. DISCUSSION AND CONCLUSIONS

Table 1 compares our work to state-of-the-art passive FTS chips reported in the literature. Most of the previous works focused on the improvement of the resolution. However, because they are constructed using silicon-based asymmetric MZIs, they suffer from a high temperature sensitivity of about 100 pm/°C [6,7,12]. Using the temperature-dependent reconstruction algorithm can reduce the temperature sensitivity, but it is only suited for a relatively small temperature range [39]. The temperature sensitivity of our method based on dual-layer waveguide interferometers is one order smaller than that

**Table 1. Comparison of Several Low Temperature Sensitivity On-Chip Spectrometers**

| Reference         | Technology  | Bandwidth (nm) | Resolution (nm) | Footprint (mm <sup>2</sup> ) | Temperature Sensitivity (pm/°C) |
|-------------------|---|----------------|-----------------|------------------------------|---------------------------------|
| [6]               | Si-SWG based MZIs   | 0.78           | 0.05            | 24                           | ~100 <sup>a</sup>               |
| [7]               | Si MZIs   | 0.6            | 0.085           | 4.5                          | ~100 <sup>a</sup>               |
| [12]              | Si MZIs   | 0.432          | 0.027           | –                            | ~100 <sup>a</sup>               |
| [39]              | Si MZIs, reconstruction algorithm                               | 0.22           | 0.017           | 23                           | –                               |
| [27]              | Si <sub>3</sub> N <sub>4</sub> /SU-8 hybrid waveguide-based MZI | 1              | 0.05            | 264                          | ~5.7 <sup>b</sup>               |
| [26] <sup>c</sup> | Tailored-SWG based MZI  | 0.76           | 0.047           | –                            | 7.5                             |
| This work         | Dual-layer Si <sub>3</sub> N <sub>4</sub> waveguide             | 7              | 0.4             | 26.68                        | ~10                             |

<sup>a</sup>Estimated from the temperature sensitivity of common Si waveguides.

<sup>b</sup>Calculated from Fig. 6 of Ref. [27].

<sup>c</sup>All the results are based on simulation.

of the conventional silicon-based FTS chips. It has a similar temperature sensitivity, compared to the other two passive compensation methods, which use negative TOC polymer in the waveguide and SWG structure to reduce the thermal phase shift [26,27]. Note that our chip is fully CMOS-compatible and the fabrication does not need high-resolution e-beam lithography. Our chip has a lower resolution compared to others, which can be enhanced by increasing the length of the dual-layer waveguides. Although the smaller group index difference of our method requires a much longer waveguide length compared to conventional MZI structures, the ER degradation is much less with the increasing OPD, and its size is still much smaller than that of the benchtop FTSs.

In this work, the FTS chip only consists of 32 waveguide interferometers, which eventually restricts the measurement points. The spectral resolution can be further improved by increasing the length of the dual-layer Si<sub>3</sub>N<sub>4</sub> waveguides, and the measurement points can be improved by increasing the number of waveguide interferometers. The chip architecture in this work used a passive power splitter to divide input light before the interferometer array. This caused the degradation of the SNR, which limits the number of interferometers. We can further improve our chip by using a tunable power splitter to replace the passive splitters or by designing a wide-area, grating-based light collection system to increase the input aperture [7]. We also can add an optical tunable filter before our FTS chip [21]. The passive FTS only retrieves a small portion of the input spectrum filtered by the optical tunable filter. By tuning the central wavelength of the filter, the whole spectrum can be reconstructed, which can greatly reduce the chip's footprint.

In summary, we have demonstrated a low temperature sensitive FTS chip based on a dual-layer Si<sub>3</sub>N<sub>4</sub> spiral waveguide array. The beating of the even and odd supermodes in the dual-layer Si<sub>3</sub>N<sub>4</sub> waveguide generates periodic fringes in the transmission spectrum. Since these two supermodes have similar modal profiles, they have a very close TOC and transmission loss, in favor of a low temperature sensitivity and a high interference ER. The measured temperature sensitivity of our chip is ~10 pm/°C, which is one order lower than that of the Si waveguide and almost half that of the single-layer Si<sub>3</sub>N<sub>4</sub> waveguide. Using such an FTS chip, we successfully reconstructed various optical spectra, including sparse laser lines and broadband optical signals, with a minimum wavelength spacing of 0.4 nm and a wavelength range of 7 nm. Since Si<sub>3</sub>N<sub>4</sub> has a wide trans-

parent wavelength range, it is possible to realize temperature-insensitive on-chip FTSs with the dual-layer Si<sub>3</sub>N<sub>4</sub> waveguide interferometers over a wide wavelength range.

**Funding.** National Natural Science Foundation of China (62075128, 62090052, 62135010).

**Acknowledgment.** The authors thank Shanghai Industrial  $\mu$ Technology Research Institute (SITRI) for the chip fabrication and SJTU-Pinghu Institute of Intelligent Optoelectronics for the chip package.

**Disclosures.** The authors declare no conflicts of interest.

**Data Availability.** Data underlying the results presented in this paper are not publicly available at this time but may be obtained from the authors upon reasonable request.

<sup>†</sup>These authors contributed equally to this work.

## REFERENCES

- Z. Yang, T. Albrow-Owen, W. Cai, and T. Hasan, "Miniaturization of optical spectrometers," *Science* **371**, eabe0722 (2021).
- A. Li, C. Yao, J. Xia, H. Wang, Q. Cheng, R. Penty, Y. Fainman, and S. Pan, "Advances in cost-effective integrated spectrometers," *Light Sci. Appl.* **11**, 174 (2022).
- R. A. Crocombe, "Portable spectroscopy," *Appl. Spectrosc.* **72**, 1701–1751 (2018).
- M. Florjanczyk, P. Cheben, S. Janz, A. Scott, B. Solheim, and D. X. Xu, "Multiaperture planar waveguide spectrometer formed by arrayed Mach-Zehnder interferometers," *Opt. Express* **15**, 18176–18189 (2007).
- K. Okamoto, H. Aoyagi, and K. Takada, "Fabrication of Fourier-transform, integrated-optic spatial heterodyne spectrometer on silica-based planar waveguide," *Opt. Lett.* **35**, 2103–2105 (2010).
- P. J. Bock, P. Cheben, A. V. Velasco, J. H. Schmid, A. Delàge, M. Florjanczyk, J. Lapointe, D.-X. Xu, M. Vachon, S. Janz, and M. L. Calvo, "Subwavelength grating Fourier-transform interferometer array in silicon-on-insulator," *Laser Photon. Rev.* **7**, L67–L70 (2013).
- T. T. D. Dinh, D. Gonzalez-Andrade, M. Montesinos-Ballester, L. Deniel, B. Szelag, X. Le Roux, E. Cassan, D. Marris-Morini, L. Vivien, P. Cheben, A. V. Velasco, and C. Alonso-Ramos, "Silicon photonic on-chip spatial heterodyne Fourier transform spectrometer exploiting the Jacquinot's advantage," *Opt. Lett.* **46**, 1341–1344 (2021).
- Z. Huang, Y. Tian, Y. Liu, H. Luo, X. Long, and C. Yu, "Optical performance monitoring using SOI-based spectral analysis," *Opt. Express* **30**, 6397–6412 (2022).



9. H. Podmore, A. Scott, P. Cheben, A. V. Velasco, J. H. Schmid, M. Vachon, and R. Lee, "Demonstration of a compressive-sensing Fourier-transform on-chip spectrometer," *Opt. Lett.* **42**, 1440–1443 (2017).
10. A. Herrero-Bermello, J. Li, M. Khazaei, Y. Grinberg, A. V. Velasco, M. Vachon, P. Cheben, L. Stankovic, V. Stankovic, D. X. Xu, J. H. Schmid, and C. Alonso-Ramos, "On-chip Fourier-transform spectrometers and machine learning: a new route to smart photonic sensors," *Opt. Lett.* **44**, 5840–5843 (2019).
11. U. Paudel and T. Rose, "Ultra-high resolution and broadband chip-scale speckle enhanced Fourier-transform spectrometer," *Opt. Express* **28**, 16469–16485 (2020).
12. H. Wang, Y. Bao, J. Tang, Q. Li, W. Shi, and X. Ma, "On-chip monolithic Fourier transform spectrometers assisted by cGAN spectral prediction," *Opt. Lett.* **46**, 4288–4291 (2021).
13. M. Nedeljkovic, A. V. Velasco, A. Z. Khokhar, A. Delage, P. Cheben, and G. Z. Mashanovich, "Mid-infrared silicon-on-insulator Fourier-transform spectrometer chip," *IEEE Photon. Technol. Lett.* **28**, 528–531 (2016).
14. T. T. Duong Dinh, X. Le Roux, N. Koopai, D. Melati, M. Montesinos-Ballester, D. Gonzalez-Andrade, P. Cheben, A. V. Velasco, E. Cassan, D. Marris-Morini, L. Vivien, and C. Alonso-Ramos, "Mid-infrared Fourier-transform spectrometer based on metamaterial lateral cladding suspended silicon waveguides," *Opt. Lett.* **47**, 810–813 (2022).
15. E. Heidari, X. Xu, C.-J. Chung, and R. T. Chen, "On-chip Fourier transform spectrometer on silicon-on-sapphire," *Opt. Lett.* **44**, 2883–2886 (2019).
16. Q. Liu, J. M. Ramirez, V. Vakarin, X. Le Roux, C. Alonso-Ramos, J. Frigerio, A. Ballabio, E. T. Simola, D. Bouville, L. Vivien, G. Isella, and D. Marris-Morini, "Integrated broadband dual-polarization Ge-rich SiGe mid-infrared Fourier-transform spectrometer," *Opt. Lett.* **43**, 5021–5024 (2018).
17. D. M. Kita, B. Miranda, D. Favela, D. Bono, J. Michon, H. Lin, T. Gu, and J. Hu, "High-performance and scalable on-chip digital Fourier transform spectroscopy," *Nat. Commun.* **9**, 4405 (2018).
18. J. Du, H. Zhang, X. Wang, W. Xu, L. Lu, J. Chen, and L. Zhou, "High-resolution on-chip Fourier transform spectrometer based on cascaded optical switches," *Opt. Lett.* **47**, 218–221 (2022).
19. R. A. Soref, F. De Leonardis, V. M. N. Passaro, and Y. Fainman, "On-chip digital Fourier-transform spectrometer using a thermo-optical Michelson grating interferometer," *J. Lightwave Technol.* **36**, 5160–5167 (2018).
20. A. Li, J. Davis, A. Grieco, N. Alshamrani, and Y. Fainman, "Fabrication-tolerant Fourier transform spectrometer on silicon with broad bandwidth and high resolution," *Photon. Res.* **8**, 219–224 (2020).
21. S. Zheng, J. Zou, H. Cai, J. Song, L. Chin, P. Liu, Z. Lin, D. Kwong, and A. Liu, "Microring resonator-assisted Fourier transform spectrometer with enhanced resolution and large bandwidth in single chip solution," *Nat. Commun.* **10**, 2349 (2019).
22. J. Li, D.-F. Lu, and Z.-M. Qi, "A modified equation for the spectral resolution of Fourier transform spectrometers," *J. Lightwave Technol.* **33**, 19–24 (2015).
23. L. J. Lu, L. J. Zhou, X. M. Sun, J. Y. Xie, Z. Zou, H. E. Zhu, X. W. Li, and J. P. Chen, "CMOS-compatible temperature-independent tunable silicon optical lattice filters," *Opt. Express* **21**, 9447–9456 (2013).
24. S. Tao, Q. Huang, L. Zhu, J. Liu, Y. Zhang, Y. Huang, Y. Wang, and J. Xia, "Athermal 4-channel (de-)multiplexer in silicon nitride fabricated at low temperature," *Photon. Res.* **6**, 686–691 (2018).
25. B. Guha, A. Gondarenko, and M. Lipson, "Minimizing temperature sensitivity of silicon Mach-Zehnder interferometers," *Opt. Express* **18**, 1879–1887 (2010).
26. U. A. Korai, A. H. Bermello, M. J. Strain, I. Giesk, and A. V. Velasco, "Design of an athermal interferometer based on tailored subwavelength metamaterials for on-chip microspectrometry," *IEEE Photon. J.* **11**, 4601611 (2019).
27. H. Podmore, A. Scott, P. Cheben, C. Sioris, P. Cameron, J. H. Schmid, A. Lohmann, Z. Corriveau, and R. Lee, "Athermal planar-waveguide Fourier-transform spectrometer for methane detection," *Opt. Express* **25**, 33018–33028 (2017).
28. L. Zhou, K. Okamoto, and S. J. B. Yoo, "Athermalizing and trimming of slotted silicon microring resonators with UV-sensitive PMMA upper-cladding," *IEEE Photon. Technol. Lett.* **21**, 1175–1177 (2009).
29. S. Feng, K. Shang, J. T. Bovington, R. Wu, B. Guan, K. T. Cheng, J. E. Bowers, and S. J. Yoo, "Athermal silicon ring resonators clad with titanium dioxide for 1.3 micron wavelength operation," *Opt. Express* **23**, 25653–25660 (2015).
30. D. Guo and T. Chu, "Compact broadband silicon 3 dB coupler based on shortcuts to adiabaticity," *Opt. Lett.* **43**, 4795–4798 (2018).
31. I. K. Kim, D. U. Kim, V. H. Nguyen, S. Han, and T. J. Seok, "High-performance and compact silicon photonic 3-dB adiabatic coupler based on shortest mode transformer method," *IEEE Photon. J.* **13**, 6601106 (2021).
32. Y. Zhang, S. Yang, A. E. Lim, G. Q. Lo, C. Galland, T. Baehr-Jones, and M. Hochberg, "A compact and low loss Y-junction for submicron silicon waveguide," *Opt. Express* **21**, 1310–1316 (2013).
33. B. Guha, J. Cardenas, and M. Lipson, "Athermal silicon microring resonators with titanium oxide cladding," *Opt. Express* **21**, 26557–26563 (2013).
34. P. Alipour, E. S. Hosseini, A. A. Eftekhari, B. Momeni, and A. Adibi, "Athermal performance in high-Q polymer-clad silicon microdisk resonators," *Opt. Lett.* **35**, 3462–3464 (2010).
35. J. T. Robinson, K. Preston, O. Painter, and M. Lipson, "First-principle derivation of gain in high-index-contrast waveguides," *Opt. Express* **16**, 16659–16669 (2008).
36. W. Gao, X. Li, L. J. Lu, J. P. Chen, and L. J. Zhou, "Broadband, low-crosstalk and power-efficient 32x32 optical switch on a dual-layer Si<sub>3</sub>N<sub>4</sub>-on-SOI platform," in *Optical Fiber Communication Conference (OFC)* (Optica Publishing Group, 2022), paper W4B.4.
37. W. Xu, Y. Guo, X. Li, C. Liu, L. Lu, J. Chen, and L. Zhou, "Fully integrated solid-state LiDAR transmitter on a multi-layer silicon-nitride-on-silicon photonic platform," *J. Lightwave Technol.* **41**, 832–840 (2023).
38. F. Vogelbacher, S. Nevlacsil, M. Sagmeister, J. Kraft, K. Unterrainer, and R. Hainberger, "Analysis of silicon nitride partial Euler waveguide bends," *Opt. Express* **27**, 31394–31406 (2019).
39. A. Herrero-Bermello, A. V. Velasco, H. Podmore, P. Cheben, J. H. Schmid, S. Janz, M. L. Calvo, D. X. Xu, A. Scott, and P. Corredera, "Temperature dependence mitigation in stationary Fourier-transform on-chip spectrometers," *Opt. Lett.* **42**, 2239–2242 (2017).